

# Mode Bifurcation and Fold Points of Complex Dispersion Curves for the Metamaterial Goubau Line

P. L. Overfelt,<sup>1</sup> Klaus Halterman,<sup>1,\*</sup> Simin Feng,<sup>1</sup> and D. R. Bowling<sup>1</sup>

<sup>1</sup>*Research and Intelligence Department, Physics Division,  
Naval Air Warfare Center, China Lake, California 93555, USA*

(Dated: February 13, 2022)

In this paper the complex dispersion curves of the four lowest-order transverse magnetic modes of a dielectric Goubau line ( $\epsilon > 0, \mu > 0$ ) are compared with those of a dispersive metamaterial Goubau line. The vastly different dispersion curve structure for the metamaterial Goubau line is characterized by unusual features such as mode bifurcation, complex fold points, both proper and improper complex modes, and merging of complex and real modes.

The Goubau line (G-Line) has been known and studied since Sommerfeld and later Goubau considered applications using non-radiating surface waves on transmission lines [1, 2]. While Sommerfeld analyzed a long cylindrical metallic wire as the transmission line of interest, Goubau realized that adding a dielectric outer sheath to the wire reduced the radial extent of the electromagnetic (EM) field and thus the dimensions of the associated excitation device. Interestingly, while the Sommerfeld wave can exist only on a conductor of finite conductivity, the Goubau wave can exist even when the inner conductor is assumed to have perfect conductivity. The G-Line has been investigated since the first part of the twentieth century, and its guided modes are well known [1, 2, 3, 4, 5]. As with all open waveguide structures, the G-Line spectrum consists of a finite discrete set of guided modes with purely real longitudinal propagation constants and an infinite continuum of radiation modes. Also present on open lossless structures are leaky waves [6, 7] characterized by discrete complex longitudinal propagation constant solutions to the dispersion equation, but which are improper solutions of Maxwell's equations in that these solutions decay longitudinally but do not obey the transverse radiation condition and thus may only be used in restricted regions of space. Improper waves are not considered part of an open waveguide spectrum and are often referred to as “nonmodal” or “nonspectral” [6]. Despite this fact, leaky waves have found great usefulness in certain applications, particularly those related to leaky wave antennas [8]. Some authors have referred to the complex solutions of the circular dielectric rod and the standard G-Line dispersion equations as *leaky modes* and have considered them on a more or less equal footing with the guided modes [9, 10]. The leaky waves of even the standard G-Line are still not well characterized (only the transverse magnetic (TM) solutions have been considered in detail [9]) but on that structure, all complex leaky wave solutions of the characteristic equation have EM field components that diverge as the radial coordinate increases to infinity and are thus improper.

In this Letter the G-Line geometry (see Fig. 1) is used with a negative index of refraction dispersive meta-

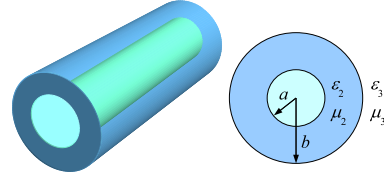


FIG. 1: Schematic of the Goubau line geometry. The metal core of radius  $a$  is a perfect conductor.

material (NIM) [11, 12] replacing the usual dielectric layer. Under these circumstances the metamaterial G-Line spectrum consists of guided modes, radiation modes, improper complex waves, and *proper* complex modes. In the following we consider only the symmetric transverse magnetic ( $\text{TM}_{0n}$ ) solutions of the metamaterial G-Line (MM G-line). The transverse electric ( $\text{TE}_{0n}$ ) and hybrid modes of the MM G-line will be considered subsequently.

Using the geometry in Fig. 1, the characteristic equation for the G-Line with perfectly conducting inner conductor and assuming a  $\theta, z, t$  dependence of  $e^{-i(m\theta + \gamma z - \omega t)}$ , can be written in the general form,

$$\bar{\gamma}^2 m^2 \left( \frac{1}{s^2} - \frac{1}{w^2} \right)^2 \mathcal{Z} \mathcal{Y} + \mathcal{S} \mathcal{T} = 0, \quad (1)$$

where  $\bar{\gamma} = \bar{\beta} + i\bar{\alpha}$  is the normalized complex longitudinal propagation constant. The longitudinal phase,  $\bar{\beta}$ , and attenuation  $\bar{\alpha}$  are both normalized by  $k_0 \equiv \omega/c$ , the free space wavenumber. Considering the  $m = 0$  case, Eq. (1) reduces to  $\mathcal{T} = 0$  for TM modes, where,

$$\mathcal{T} = \frac{\epsilon_2 \mathcal{W}}{w} - \epsilon_3 \mathcal{Z} g = 0, \quad (2)$$

$\mathcal{S} = \mu_2 \mathcal{X}/w - \mu_3 \mathcal{Y} g$ , and  $g \equiv -H_1^{(2)}(s)/(sH_0^{(2)}(s))$ . We also define,  $\mathcal{Z} = J_0(w)Y_0(v) - J_0(v)Y_0(w)$ ,  $\mathcal{Y} = -J_0(w)Y_1(v) + J_1(v)Y_0(w)$ ,  $\mathcal{W} = -J_1(w)Y_0(v) + J_0(v)Y_1(w)$ , and  $\mathcal{X} = J_1(w)Y_1(v) - J_1(v)Y_1(w)$ , with the  $J$ 's,  $Y$ 's and  $H$ 's the usual Bessel functions of the first and second kind, and the Hankel functions of the second kind, respectively. The dimensionless wavenumbers are,  $v = k_2 a$ ,  $w = k_2 b$ , and  $s = k_3 b$ . The transverse propagation wave numbers are given by  $k_j = k_0 \sqrt{\epsilon_j \mu_j - \bar{\gamma}^2}$ , for

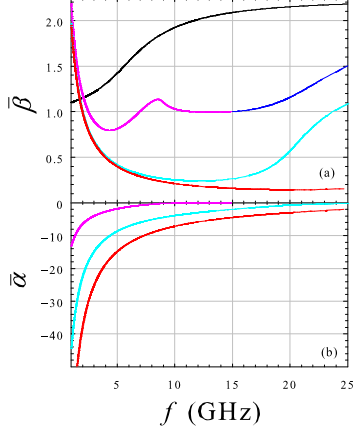


FIG. 2: Dispersion for standard G-line

$j = 2, 3$ . For these TM<sub>0n</sub> modes, the EM fields in the  $j$ th region are generally written as,  $\mathbf{H}_j = H_{j,\theta} \hat{\theta} e^{-i(\gamma z - \omega t)}$ , and  $\mathbf{E}_j = (E_{j,\rho} \hat{\rho} + E_{j,z} \hat{z}) e^{-i(\gamma z - \omega t)}$ , for propagation in the positive  $z$  direction. Maxwell's equations and the cylindrical symmetry result in the following transverse fields,  $H_{j,\theta} = -i\epsilon_j k_0 / \kappa_j^2 \partial E_{j,z} / \partial \rho$ , and  $E_{j,\rho} = -i\gamma / \kappa_j^2 \partial E_{j,z} / \partial \rho$ . The forms of (1) - (2) above are most suitable for emphasizing material parameter changes in both  $\epsilon$  and  $\mu$  of Regions 2 and 3, although they have been derived previously in alternate forms [5].

We solve Eq. (2) numerically for its complex zeros as a function of frequency by employing a recently developed complex root finding algorithm. Fig. 2 shows the four lowest-order TM<sub>0n</sub> ( $n = 0, 1, 2, 3$ ) modes as functions of frequency (in GHz) for the standard G-Line. Part (a) shows the normalized longitudinal phase vs. frequency while Part (b) shows normalized longitudinal attenuation vs. frequency. In Fig. 2 the parameters  $\epsilon_2 = 5$ ,  $\mu_2 = 1$ ,  $a = 5$  mm,  $b = 10$  mm were used to compare our results with those in Ref. 9. In particular, note the lowest-order TM<sub>00</sub> mode (black curve) that has no cutoff frequency and  $\alpha = 0$ . Except for this mode, our results are consistent with Ref. 9. We have assumed that the outside region is air and thus  $\epsilon_3 = \mu_3 = 1$ . At a given frequency, when the imaginary part of a root is zero, that root represents a guided or bound solution. When the imaginary part is nonzero, that root represents a complex leaky wave solution of (2). Upon calculating the EM field components associated with certain leaky wave solutions in Fig. 2, all discrete complex solutions of the standard G-line (with Region 2 index of refraction greater than one) are improper [6, 9]. Because the outside region is air, cutoff occurs when  $\bar{\gamma} = 1$  or  $s = 0$ . When  $1 < \bar{\beta} < \sqrt{5}$ , and  $\bar{\alpha} = 0$ , the well-known guided modes result. When  $\bar{\beta} < 1$ ,  $\bar{\alpha} \neq 0$ , the waves are leaky. Also note that an infinite number of higher order leaky waves can occur at lower frequencies. These leaky waves have high frequency cutoffs but no low frequency cutoffs. Generally these

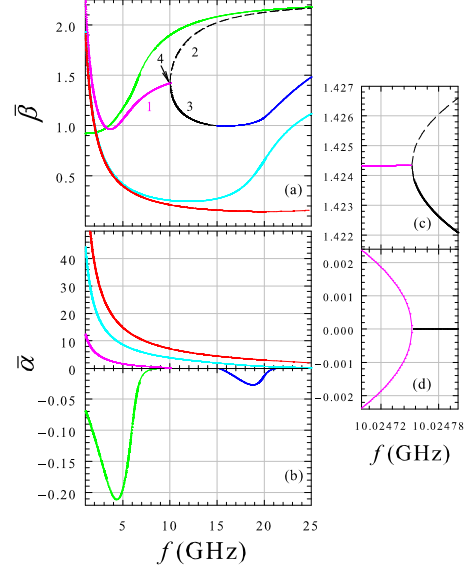


FIG. 3: Dispersion for the MM G-line. The curves in (c) and (d) give a magnified view of  $\bar{\beta}$  and  $\bar{\alpha}$ , respectively, near the bifurcation point (Point 4).

waves have  $|\bar{\alpha}| \gg 1$  and thus are not so far found to be particularly useful. In Fig. 2, the real and imaginary parts of the longitudinal propagation constant are correlated using color. Thus the lowest-order mode (black) has zero attenuation and is purely guided [Fig. 2(a)], the second lowest-order mode (magenta) is leaky at the lower frequencies with its attenuation magnitude increasing as the frequency decreases (see Fig. 2(a) and (b)). For this mode as the frequency increases up to cutoff at about 14.9 GHz, the associated attenuation decreases in magnitude until this mode becomes a guided mode once cutoff is passed (magenta  $\rightarrow$  blue). The turquoise blue and red curves show the next higher-order modes which for much of the frequency range are leaky with  $|\alpha| \gg 1$ .

If the dielectric layer of Region 2 is replaced by a negative index of refraction MM, the TM mode structure is vastly different. The MM is characterized by the following dispersion formulas,  $\mu_2(f) = \mu_l + F f^2 / (f_0^2 - f^2 - i\Gamma f)$ , and,  $\epsilon_2(f) = \epsilon_h + f_p^2 / (f_r^2 - f^2 - i\Gamma f)$ . We take the filling factor,  $F$ , to be 0.25, and the damping factor,  $\Gamma$ , to be zero. The low and high frequency limits are  $\mu_l = -1$  and  $\epsilon_h = -5$ , respectively. The resonance frequencies are,  $f_0 = 0.75$  GHz,  $f_r = 0.5$  GHz, and  $f_p = 0.25$  GHz.

Figure 3 contains the four lowest-order TM modes assuming a metamaterial G-Line with both  $\epsilon_2$  and  $\mu_2$  negative over the frequency range of interest. Fig. 3(a) shows the normalized longitudinal phase vs. frequency, part (b) shows the normalized longitudinal attenuation vs. frequency, where  $|\bar{\alpha}|$  is small, and also shows the normalized longitudinal attenuation on a larger scale. In Fig. 3,  $\epsilon_2 \approx -5$  and  $\mu_2 \approx -1$ . The radii,  $a$  and  $b$ , are the same

as for the standard G-line in Fig. 2. Referring to the various mode “paths” or “branches” in Fig. 3, note that the green curve now has a leaky part (below about 3 GHz) and the portion of the green curve with  $\bar{\beta} > 1$  now has  $\bar{\alpha} \neq 0$ . As the frequency decreases, the attenuation peaks in magnitude between 4 and 5 GHz (green curve) and then starts to decrease. Thus the green path is a wave with a complex  $\bar{\gamma}$ . This path is also improper (until it merges with the black curves at much higher frequency). Thus the fundamental guided mode of the standard G-line is replaced by a complex mode that is improper. The mode represented by the magenta path is also complex with  $\bar{\alpha}$  nonzero until point 4 is reached. However this path is proper. At point 4 ( $f \approx 10.025$  GHz), there is a mode bifurcation [see Fig. 3(c) and (d)], as has been observed in catastrophe and bifurcation theories. Catastrophe theory attempts to study how the qualitative nature of solutions of equations depends on the parameters appearing in those equations [14, 16]. These techniques are invaluable in analyzing the qualitative changes in system dynamical characteristics by small perturbations. From this standpoint, the dispersion relationship,  $\mathcal{T} = 0$ , is cast as a nonlinear equation in  $\bar{\beta}$ ,  $\bar{\alpha}$ , and  $f$  with parameters  $\epsilon_1$ ,  $\epsilon_2$ ,  $\mu_1$ ,  $\mu_2$ ,  $a$ , and  $b$ . Using catastrophe theory, areas of unusual qualitative interest such as the fold point at Point 4 can be determined. Using numerical techniques alone to solve the dispersion relation over a frequency range is difficult due to its “dense” set of zeros at each frequency. Point 4 is a complex fold point (a point where, because no material losses in the line have been assumed as yet,  $\bar{\gamma}$ ,  $-\bar{\gamma}$ ,  $\bar{\gamma}^*$ , and  $-\bar{\gamma}^*$  all meet at the same frequency) [13, 14, 15, 16]. As the frequency increases past the fold point,  $\bar{\alpha} \rightarrow 0$  along both upper and lower black paths. The black paths near points 2 and 3 are therefore both guided modes immediately after bifurcation.

Thus, in Fig. 3 there are an improper complex set of roots, a proper complex set of roots, and a mode bifurcation at a fold point in (a) near  $f \approx 10$  GHz past which there are two guided modes (i.e.,  $\bar{\alpha} = 0$  on both black paths after 10 GHz). By considering the two guided paths (2 and 3) where  $\bar{\alpha} = 0$ , we find that the black upper path always has a slope opposite in sign to the lower path until the first cutoff frequency,  $f \approx 14.9$  GHz, and thus is backward traveling in this frequency region. At cutoff the lower path near point 3 has zero slope and after cutoff, the slope becomes positive. Also after cutoff, this path becomes complex with  $|\bar{\alpha}| \ll 1$ , as shown by the blue curve in Fig. 3(b). The red and turquoise blue curves are quite similar to those in Fig. 2 over the given frequency range but they, too, exhibit the bifurcation and fold point phenomena at higher frequencies. None of the above situations occur for the standard G-line.

Certain effects similar to those in Fig. 3 have been seen in both grounded metamaterial slab geometries [17, 18] and in complicated grounded dielectric-loaded, open ge-

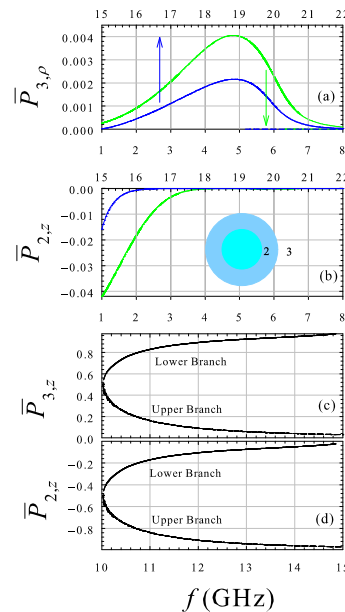


FIG. 4: Normalized power (see text) as a function of frequency for a few of the dispersion curves in Fig. 3, and using the same color scheme. In (a), the radial power flux increases, consistent with the attenuation growth for the mode. In (b), the longitudinal power flux in the MM region declines rapidly with frequency. The modes in (c) and (d) are strictly guided, with the EM energy flowing in the MM mainly for those modes in the upper branch of the dispersion curve of Fig. 3.

ometries [13, 19, 20, 21, 22]. In the case of the MM G-line, we have a transition from a complex proper mode (magenta curve in Fig. 3(a)) to a pair of guided modes at higher frequencies. We see in both the normalized phase and attenuation the characteristic intersection of a parabola and a straight line [Fig. 3(c) and (d)]. The phase has a straight line to parabola transition characteristic of a fold point in catastrophe theory [13, 14, 15, 16]. Note that the attenuation for the MM G-line in Fig. 3(b) has changed sign for the red, magenta, and turquoise blue curves when compared to the standard G-line, while the attenuation shows a parabola to straight line transition.

The guided and leaky modes of the G-line and MM G-line can be described as slow modes and fast modes, respectively. The guided modes are slow in that they occur in the spectral region  $\sqrt{\epsilon_3\mu_3} < \bar{\beta} < \sqrt{\epsilon_2\mu_2}$ . Since  $\bar{\beta} > 1$ ,  $c\beta/\omega > 1$  but  $\omega/(c\beta) < 1$ , thus their phase velocity is less than the speed of light. In contrast the leaky waves are fast waves. Note that with reference to both Fig. 2 and Fig. 3 there is a point at the low frequency end of each graph where (although we cut the graphs off at  $\sqrt{\epsilon_2\mu_2}$ ) there are complex solutions of the dispersion relation that have  $\bar{\beta} > \sqrt{\epsilon_2\mu_2}$ , and  $\bar{\alpha} \neq 0$ . For the standard G-line this region is a “forbidden” region. For the MM G-line of Fig. 3,  $\bar{\beta} > \sqrt{\epsilon_2\mu_2}$  is no longer considered forbidden, and “superslow modes” can arise [12].

The total power through the various regions can be described by the normalized power in the radial and longitudinal directions,  $\bar{P}_{j,\sigma} = P_{j,\sigma}/P_{\text{tot}}$ , for  $\sigma = \rho, z$ , and  $j = 2$  or  $3$ . The total power,  $P_{\text{tot}}$  is the sum of power flux, defined as,  $P_{\text{tot}} \equiv \sum_{j,\sigma} |P_{j,\sigma}|$ . The power flux through the surface of a cylinder of radius  $R$  and length  $L$  encompassing a segment of the structure is determined from the spatially integrated time-averaged Poynting vector  $\mathbf{S}_j$ , with components,  $S_{j,z}(\rho, z) = (c/8\pi)e^{2\alpha z}\text{Re}[E_{j,\rho}H_{j,\theta}^*]$ , or  $S_{3,\rho}(\rho, z) = -(c/8\pi)e^{2\alpha z}\text{Re}[E_{3,z}H_{3,\theta}^*]$ . Thus, the longitudinal power transmitted through the two circular regions is,  $P_{j,z}|_{z=L} = 2\pi e^{2\alpha L} \int_0^R \rho d\rho S_{j,z}(\rho, 0)$ , and  $P_{j,z}|_{z=0} = -2\pi \int_0^R \rho d\rho S_{j,z}(\rho, 0)$ . For the surface normal to  $\hat{\rho}$ , integration gives,  $P_{3,\rho} = 2\pi R e^{\alpha L} (1/\alpha) \sinh(\alpha L) S_{3,\rho}(R, 0)$ . We take  $R/b = 10$ . In Fig. 4, we illustrate the normalized power as a function of frequency for several of the modes shown in Fig. 3. In panel (a), power flows radially, with maxima at frequencies correlated to when  $|\alpha|$  peaks for that mode (Fig. 3(b)). Although the power flow is predominately in the air region, it is evident that the counter-directed longitudinal power flux in the MM region declines rapidly towards zero with increased frequency [panel (b)]. This indicates that power emission from the waveguide takes place at a slight angle,  $\vartheta$  from the  $z$  axis over a relatively small bandwidth. As for the proper mode spectra,  $|\bar{P}_{j,z}| = 1/2$  for both regions, but counter-directed. At the bifurcation point ( $f \approx 10$  GHz), the leaky wave transforms into a strictly guided mode at higher frequencies, where the two counter propagating regions are clearly identified by their sign [Fig. 4(c) and (d)]. The lower branch (see Fig. 3) in the guided mode dispersion clearly maps to power flow that is predominately in the air region. This is in contrast to modes occupying the upper branch in Fig. 3, where again in Fig. 4(c) and (d) we see the power distribution shift from both regions equally to reside completely in the MM at higher frequencies. This also verifies that the MM G-line has the remarkable property that certain guided modes can propagate below the first waveguide cutoff and can be of the backward as well as of the forward wave type [23, 24, 25].

In conclusion, dispersion curve behavior for a dielectric versus MM G-Line has been shown to be vastly different. The MM G-line dispersion is characterized by unusual mode bifurcations, complex fold points a la catastrophe theory, and both proper and improper complex modes.

The authors acknowledge G. A. Lindsay, Z. Sechrist, and G. Ostrom for valuable discussions and the support from ONR, as well as NAVAIR's ILIR program from ONR. This work is also supported in part by a grant of HPC resources as part of the DOD HPCMP.

- 
- \* Electronic address: klaus.halterman@navy.mil
- [1] A. Sommerfeld, *Ann. Physik* **15**, 673 (1904); G. Goubau, *J. Appl. Phys.* **21**, 1119 (1950).
  - [2] G. Goubau, *IRE Trans. Antennas Propag.* **7**, S140 (1959).
  - [3] J. A. Stratton, *Electromagnetic Theory* (McGraw-Hill, New York, 1941).
  - [4] R. A. Waldron, *Theory of Guided Electromagnetic Waves* (Van Nostrand Reinhold, London, 1969).
  - [5] N. A. Semenov, *Radio Eng. Electr. Phys.* **9**, 989 (1964); J. G. Fikioris and J. A. Roumeliotis, *IEEE Trans. Microwave Theory Tech.* **27**, 570 (1979); K. Sakina and J. Chiba, *IEICE Trans. Electron.* **76**, 657 (1993).
  - [6] N. Marcuvitz, *IRE Trans. Antennas Propag.* **4**, 192 (1956); T. Tamir and A. A. Oliner, *Proc. IEE* **110**, 310 (1963).
  - [7] D. Marcuse, *Theory of Dielectric Optical Waveguides* (Academic Press, Orlando, FL, 1974); A. W. Snyder, *Appl. Phys.* **4**, 273 (1974).
  - [8] L. O. Goldstone and A. A. Oliner, *IRE Trans. Antennas Propag.* **XX**, 307 (1958 or 1959); R. E. Collin and F. J. Zucker, *Antenna Theory, Part 2* (McGraw-Hill Book Company, New York, 1969); R. C. Johnson, *Antenna Engineering Handbook* (McGraw-Hill Book Company, New York, 1993) Third Edition, Chapter 10; R. E. Collin, *Field Theory of Guided Waves, 2nd ed.* (New York, IEEE Press, 1991); A. Alu, et al., *IEEE Trans. Antennas Propag.* **55**, 1698 (2007).
  - [9] K. Y. Kim, *Microwave Opt. Tech. Lett.* **50**, 523 (2008);
  - [10] K. Y. Kim, et al., *Electr. Lett.* **39**, 61 (2003); K. Y. Kim, *Guided and Leaky Modes of Circular Open Electromagnetic Waveguides*, PhD Thesis (2004).
  - [11] G. V. Eleftheriades and K. G. Balmain, *Negative Refraction Metamaterials* (IEEE Press, Hoboken, NJ, 2005); N. Engheta and R. W. Ziolkowski, *Metamaterials* (IEEE Press, Hoboken, NJ, 2006).
  - [12] I. V. Shadrivov, et al., *Phys. Rev. E* **67**, 057602 (2003); K. Halterman, et al., *Phys. Rev. A* **76**, 013834 (2007).
  - [13] A. B. Yakovlev and G. W. Hanson, *IEEE Trans. Microwave Theory Tech.* **45**, 87 (1997).
  - [14] G. W. Hanson and A. B. Yakovlev, *Radio Science* **33**, 803 (1998).
  - [15] I. E. Pochanina, et al., *Radiofizika* **32**, 1000 (1989).
  - [16] T. Poston and I. Stewart, *Catastrophe Theory and Its Applications* (London, Pitman, 1978); R. Gilmore, *Catastrophe Theory for Scientists and Engineers* (New York, Wiley, 1981).
  - [17] W. Shu and J. M. Song, *PIER* **65**, 103 (2006).
  - [18] G. Lovat, et al., *Metamaterials* **34** (2008), doi:10.1016/j.metmat.2008.09.002.
  - [19] P. Baccarelli, et al., *IEEE Trans. Microwave Theory Tech.* **53**, 32 (2005).
  - [20] P. Lampariello, et al., *IEEE Trans. Microwave Theory Tech.* **38**, 1831 (1990).
  - [21] S. Majumder, et al., *IEEE Trans. Microwave Theory Tech.* **45**, 2296 (1997).
  - [22] T. Tamir and F. Y. Kou, *IEEE J. Quantum Electr.* **22**, 544 (1986).
  - [23] S. Hrabar and G. Jankovic, *IEEE MELECON*, 280, Malaga, Spain, May 16-19 (2006).
  - [24] S. Hrabar, et al., *IEEE Trans. Antennas Propag.* **53**, 110

- (2005).
- [25] G. Lubkowski, *et al.*, IET Microwave Antennas Propag. **1**, 165 (2007).